Planetary and Space Science 179 (2019) 104725

Contents lists available at ScienceDirect

Planetary and Space Science

journal homepage: www.elsevier.com/locate/pss

Ablation of Ni from micrometeoroids in the upper atmosphere: Experimental and computer simulations and implications for Fe ablation

David L. Bones [a,*], Juan Diego Carrillo-Sánchez [a], Alexander N. Kulak [a], John M.C. Plane [a,**]

[a] School of Chemistry, University of Leeds, Leeds, UK

ARTICLE INFO

Keywords:
Micrometeoroid
Mesosphere
Ablation
Nickel
Iron
Cosmic dust

ABSTRACT

Modelling the ablation of Ni from micrometeoroids upon their entry to the Earth's atmosphere enables us to better understand not just the Ni layers in the upper atmosphere but also the differential ablation of Fe. A new version of our meteoroid ablation model has been developed that includes a metal phase in addition to the existing silicate phase. The validity of this new model has been verified via laboratory experiments of Ni ablation. Meteoritic particles (powdered terrestrial meteorites) and mineral proxies were flash heated to temperatures as high as 2700 K to simulate atmospheric entry. Slower linear heating ramps were also conducted to allow a more precise study of ablation as a function of temperature. Ni ablates rapidly, shortly after Na, which was used here as a reference. The model reproduces the experimental results generally within experimental error. Disagreement between the model and the data can be explained by the distribution of Ni in small grains in the meteorite samples, in contrast to the model assumptions of one molten metal phase. Small grain sizes are consistent with the Fe–Ni grain size observed in SEM-EDX mapping of the meteorite particles used for this study.

1. Introduction

Of the roughly 40 tonnes of cosmic dust that enters the Earth's atmosphere every day (Carrillo-Sánchez et al., 2016), the majority are Fe-containing silicate minerals such as olivine and pyroxene. A minor fraction, estimated at about 9 wt% (Fredriksson and Kerridge, 1988), of the mass is Fe–Ni sulfide, including pyrrhotite, troilite and pentlandite. Metallic Fe–Ni is an even smaller percentage, probably around 1.5%. The various elements in meteoroids ablate differentially upon atmospheric entry, that is, they ablate at different altitudes and to different extents. Volatile elements like Na ablate earlier (higher in the atmosphere) and to a greater extent than refractory elements like Ca. The ablated metal atoms contribute to layers of metal and metal ions that form in planetary atmospheres close to the 1 μbar pressure level (e.g. 90 km on Earth, 120 km on Venus and 80 km on Mars) (Plane, 2003). These layers provide a sensitive probe of transport and dynamics in the mesosphere (Plane et al., 2015) and also generate meteoritic smoke particles which are thought to provide condensation nuclei for polar mesospheric cloud formation (Wilms et al., 2016). When concentrated by electrodynamic forces into concentrated layers of metal ions (termed sporadic *E* layers), the associated electron densities can be high enough to reflect medium and short radio wavelengths, thus impacting on both terrestrial and satellite radio communications (Pavlov, 2012).

A Chemical Ablation Model (CABMOD) has been developed at the University of Leeds to simulate the ablation of metals from micrometeoroids entering a planetary atmosphere. This includes not just the terrestrial planets but also satellites of the gas giants and the gas giants themselves. CABMOD can simulate the entry of particles up to 5 mg in mass, moving at any specified velocity. Up until now, this model has assumed that Fe was only present in the silicate phase as FeO and ablated late in the descent (Vondrak et al., 2008). Metallic Fe or Fe in Fe–Ni sulfide will evaporate at lower temperatures than Fe in silicate phases, so it will ablate both to a greater extent and higher up than silicate Fe (Gómez-Martín et al., 2017).

1.1. Scope of article

The differential ablation of Fe–Ni sulfide can be approximated from the ablation of metallic Fe–Ni. Most of the S is lost early in the particle's descent as S evaporates from the Fe–Ni–S solid leaving just the metallic phase (Walder and Pelton, 2005). By measuring the ablation of Ni from meteoritic material experimentally, we can combine this data with

---

[*] Corresponding author.
[**] Corresponding author.
E-mail addresses: D.L.Bones@leeds.ac.uk (D.L. Bones), J.M.C.Plane@leeds.ac.uk (J.M.C. Plane).

https://doi.org/10.1016/j.pss.2019.104725
Received 20 December 2018; Received in revised form 15 August 2019; Accepted 16 August 2019

previous laboratory measurements of Fe ablation to improve CABMOD to include the ablation of metallic Fe–Ni and Fe–Ni sulfide.

In this paper, we explore the differential ablation of Ni using the Meteoric Ablation Simulator (MASI), a laboratory-based experiment where micron-sized meteoritic particles are rapidly heated to simulate the temperatures of atmospheric entry. Evaporating metals are detected in real time with Laser Induced Fluorescence (LIF). We then describe the development of a new version of CABMOD to account for the ablation of Ni, as well as previously reported MASI data on Fe ablation (Gómez-Martín et al., 2017).

1.2. Fe and Ni layers in the mesosphere

The existence of Fe and Fe^+ layers in the Earth's mesosphere and the physical and chemical processes involved in their production are well known (Feng et al., 2013; Plane et al., 2015). Recently, a Ni layer has also been detected in the mesosphere by resonance lidar (Collins et al., 2015; Gerding et al., 2018). The ratio of Fe to Ni was estimated to be 1.2 from the 2015 lidar measurements, much lower than the Fe:Ni ratio of 18 based on the elemental abundance of Ni in carbonaceous Ivuna (CI) chondrites (Lodders and Fegley, 2011). More recent lidar measurements suggest an Fe:Ni ratio very close to this higher CI ratio (Gerding et al., 2018). The Ni layer extends nearly 10 km lower in the terrestrial atmosphere than the Fe or Na layers, and may thus provide a probe of the middle mesosphere.

1.3. Ni and Fe–Ni-sulfide in cosmic dust

The composition of the cosmic dust entering the Earth's atmosphere is thought to be similar to that of CI chondritic meteorites (Schramm et al., 1989; Taylor et al., 2012; Noguchi et al., 2015), a rare class of meteorites that have become a reference standard for the solar system (Lodders and Fegley, 2011; Grady et al., 2014). They are thought to best represent the material present in the early solar system. The majority (~90% by mass) of cosmic dust particles that intercept the Earth are thought to originate from Jupiter Family Comets (Nesvorny et al., 2010; Carrillo-Sánchez et al., 2016).

The remaining 10% of cosmic dust particles will be asteroidal in origin. They tend to be larger (50–400 μm) and to have slower entry velocities. These particles, therefore, make up the bulk of recovered micrometeorites. Their compositions are closer to that of carbonaceous Mighei (CM) chondrites than those of carbonaceous Vigarano (CV) chondrites or ordinary chondrites (Kurat et al., 1994; Taylor et al., 2012).

The composition of cosmic dust is primarily inferred from empirical investigation of Earth-recovered Antarctic and deep-sea micrometeorites. These particles are likely to have undergone some thermal processing on their descent through the atmosphere as well as terrestrial weathering once at the Earth's surface. Antarctic micrometeorites derived from blue-ice or snow are least altered by terrestrial weathering and are considered fairly pristine; once the particle is embedded in ice or snow it is protected from terrestrial weather (Dobrica et al., 2012; Noguchi et al., 2015, 2017). Additionally, Interplanetary Dust Particles (IDPs) have been collected in the stratosphere (Levasseur-Regourd et al., 2018). Cometary particles have also been collected in space: the Vega mission to comet 1P/Halley; the Stardust mission to comet 81P/Wild 2; and the Rosetta mission to 67P/Churyumov–Gerasimenko. The cometary particles collected in interplanetary space were on the whole similar in elemental abundances to CI and CM chondrites. Wild 2 particles had very small amounts of Ni: just two grains of pentlandite were detected (Zolensky et al., 2006). The Rosetta particles showed Ni:Fe ratios similar to those found in carbonaceous chondrites, such as the Allende meteorite (Stenzel et al., 2017) although, according to Hilchenbach et al. (2016), the particles seem to be consistently enriched in Fe which suggested higher than chondritic levels of FeS, and Na was also enriched by a factor of 4.8 ± 3.7 (Hilchenbach et al., 2016).

Micrometeorites are the remnants of micrometeoroids that have deposited on the Earth's surface (Genge et al., 2008). They have typically undergone considerable melting and fractionation with loss of the more volatile components (S, Na, K, metallic Fe, Ni), though some Ni is incorporated into olivine that crystallises as the particle cools back down (Cordier et al., 2011). In meteoroids with a significant amount of carbon (e.g., CM and CI type carbonaceous chondrites), the rapid pyrolysis of the carbon could produce reducing conditions (Genge and Grady, 1998; Cordier et al., 2011; Court and Tan, 2016), enabling reactions such as:

$$C + 2FeO \rightarrow 2Fe + CO_2 \tag{1}$$

Siderophile elements such as Fe and Ni are even less miscible in this reduced silicate melt and are segregated. The metal sulfide melts coalesce and migrate to the surface, from where they can evaporate (Alexander et al., 2002; Taylor et al., 2011). FeNi beads enriched in Ni have been observed at the surface of micrometeorites. It is likely that these are the remnants of a (Fe,Ni)S phase that migrated to the surface, then lost S and Fe (Taylor et al., 2011).

Scoriaceous cosmic spherules are a subgroup of micrometeorites that have undergone partial melting before being deposited on the Earth's surface, losing their original texture in the process and being left with internal cavities formed by the evaporation of volatiles (Genge et al., 2008). Analyses of micrometeorites collected in Antarctica show an overall composition similar to CM or CR chondrites, with significant depletion in S, Na and Ni (Kurat et al., 1994; Taylor et al., 2000).

2. Experimental methods

2.1. Experimental setup

The experimental setup of the MASI has been described previously (Bones et al., 2016; Gómez-Martín et al., 2017). Briefly, particles chosen as micrometeoroid proxies are placed on a ribbon of tungsten in a chamber at a pressure of 0.6 Torr in a flow of N_2 (60 sccm). The W filament is resistively heated to temperatures as high as 2873 K. The filament temperature is monitored by a pyrometer with a temperature range of 1273–2873 K and a less than 10 ms response time (System 4 Ratio Thermometer, Land Instruments). A programmable power supply (ES 015-10 Delta Electronika) controls the current through the filament, delivering very close approximations to calculated atmospheric entry temperature profiles via a proportional-integral-derivative algorithm. This allows a time resolution of tens of milliseconds.

The relative concentrations of two metals can be measured simultaneously via time-resolved LIF. Evaporated metal atoms (here, Ni and the reference metal, Na) are excited by probe beams from two dye lasers tuned to 336.954 and 588.995 nm for Ni and Na, respectively. The resonance fluorescence is detected orthogonally through small monochromators (4 nm resolution) coupled to photomultiplier tubes. This is essentially the set up used to measure the evaporation of Fe, Mg and Ca in previous experiments (Bones et al., 2016, 2018; Gómez-Martín et al., 2017). The 337 nm dye laser is pumped at 250 Hz by a Litron TRL-nano 50–250 Nd-YAG laser whilst the 589 nm dye laser is pumped at 10 Hz by a Continuum Minilite Nd-YAG laser.

2.2. Samples

Ground samples of two meteorites were used: Allende, a CV3 carbonaceous chondrite and Chergach, an H5 ordinary chondrite. After grinding, the particles from both meteorites were size separated by sieve. It should be noted that these particles are likely to be aggregates and hence highly inhomogeneous in composition, which was confirmed by Scanning Electron Microscope-Energy Dispersive X-ray (SEM-EDX) analysis (see section 3.1 for a detailed description of sample mineralogy).

FeNi alloy powder (50:50 wt %, Alfa Aesar, particle radius less than 22 μm) was used as received. A sample of pentlandite (Sudbury, Ontario, Canada) was magnetically separated from the surrounding breccia matrix after grinding. The resulting flakes were 10–400 μm in radius.

The morphologies of the particles were determined using scanning electron microscopy (SEM), where the particles were mounted on an SEM stub using an adhesive carbon tape. Samples were then imaged using a FEI Nova NanoSEM 450 operating at 3 kV, without coating, using deceleration mode and a circular backscatter (CBS) detector. The elemental energy-dispersive X-ray spectroscopy (EDX) analysis was conducted by an EDAX (Ametek) with the SEM operating at 18 kV. The default standard-less setting was used.

2.3. The Chemical Ablation Model (CABMOD)

In essence, CABMOD solves the energy and momentum equations to predict the thermal heating of the particle from collisions with air molecules (Vondrak et al., 2008). Assuming Langmuir evaporation, it uses the vapor pressure calculated by the MAGMA thermodynamic code (Fegley and Cameron, 1987; Schaefer and Fegley, 2005) to determine the evaporation rate of each element as a function of altitude, iteratively accounting for changes in the particle mass and composition.

For the present study, CABMOD has been extended to include a separate Fe–Ni phase which is treated as if chemically separate from the silicate phase(s) that comprise the rest of the micrometeoroid. Using the thermodynamic data for Fe–Ni melts, the ablation of the Fe–Ni phase can be predicted by considering the metal phase as coexisting with the silicate phase of an ablating particle. In the model, the ablation of each phase does not affect the other in a chemical sense, but is taken into account with respect to changes in mass and volume and hence temperature of the particle. This model is realistic in the sense that the immiscible silicate and sulfide phases are known to have separated out in micrometeorites, leaving FeS blebs or FeNi beads on the surface. In fact, sulfur evaporates faster than Fe and Ni so FeNi beads are often all that remains of an Fe–Ni–S phase (Taylor et al., 2011).

2.3.1. The earlier version of CABMOD (CABMOD-2)

Both the original (CABMOD-2) and the new (CABMOD-3) versions of CABMOD iteratively solve the momentum and thermal energy balance of atoms and molecules ablating from micrometeoroids entering the earth's atmosphere. Sputtering (mass loss caused by hyperthermal collisions between the incoming particles and air molecules (Tielens et al., 1994)) is included in CABMOD but has a negligible impact on the relatively volatile metals studied here. It is also not relevant for comparing MASI experimental results with the corresponding CABMOD simulations. Other processes such as fragmentation are not included in either version of CABMOD.

At the melting point, or more accurately, the melting range of the particle, the micrometeoroid begins ablating as the molten metals and metal oxides rapidly evaporate. Cosmic dust particles are at least as heterogeneous as the meteorite analogues discussed in Section 2. They include silicate minerals such as olivine and pyroxene as well as sulfides and metal alloys. For simplicity, CABMOD-2 assumed micrometeoroids are homogeneously composed of a mixture of oxides (Na_2O, K_2O, FeO, SiO_2, MgO, Al_2O_3, TiO_2 and CaO) with an overall Forsterite olivine ($Mg_{1.1}Fe_{0.9}SiO_4$) composition. The rate of evaporation is determined by the Hertz-Knudsen equation:

$$\frac{dm_i}{dt} = f(T)\gamma_i p_i S\sqrt{\frac{M_i}{2\pi k_B T}} \tag{2}$$

where S is the surface area of the particle, T the temperature, k_B is Boltzmann's constant, p_i is the gas-liquid equilibrium vapor pressure, γ_i is the evaporation coefficient (or sticking coefficient), and $f(T)$ is the phase transition factor that accounts for non-instantaneous melting.

The evaporation coefficient γ_i is assumed to be 1 for all compounds, both for simplicity and also due to a lack of experimental data. The phase transition factor is represented as a sigmoidal function:

$$f(T) = \frac{1}{1+\exp\left(\frac{-(T-T_{mp})}{\tau}\right)}, \tag{3}$$

where T_{mp} is the average melting point of the assumed homogeneous phase, and τ represents the width of the sigmoid profile. This allows for melting over a range of temperatures, with the most rapid melting occurring at T_{mp}. We have previously assumed $T_{mp} = 1800$ K, corresponding to the melting point of Fo_{56} olivine (i.e., 56mol% Forsterite, Mg_2SiO_4 and 44mol% Fayalite, Fe_2SiO_4) (Vondrak et al., 2008). This melting point was estimated from the phase diagram for olivine (Bowen and Schairer, 1935; Swartzendruber et al., 1991). Fo_{56} olivine corresponds to the bulk composition of CI chondrites (Lodders and Fegley, 2011). The Fe:Mg ratio in Allende is similar to the ratio in CI chondrites so 1800 K was used as the melting point for ablation simulations concerning particles of both CI composition and from Allende. The Fe:Mg ratio in Chergach requires a melting temperature of 1960 K in particle ablation simulations. The parameter τ was calibrated from previous experimental measurements to be 51 K for Allende and similar carbonaceous chondrites and 108 K for ordinary chondrites such as Chergach (Gómez-Martín et al., 2017).

In our previous studies of Na, Fe and Ca ablation we concluded that including a pure metal phase separate to the bulk silicate phase would account for an early release of Fe that was observed in heating ramps conducted with MASI, evident as a double peaked ablation profile (Gómez-Martín et al., 2017). Double peaked profiles were common for meteoritic analogues like Chergach with a high abundance of metallic Fe. CABMOD-2 could only reproduce the second, higher temperature ablation profile peak corresponding to silicate Fe.

2.3.2. CABMOD-3: CABMOD with immiscible metal phase

CABMOD-3 assumes two immiscible phases, silicate and metal. This is reasonable given the large immiscibility gap in the Fe–S–Si system (Sanloup and Fei, 2004). Density differences promote further separation in the molten particle as the heavier metal phase sinks and the silicate phase floats. The silicate bulk density is 2200 kg m^{-3} (Consolmagno et al., 2008), while a density of 4710 kg m^{-3} is characteristic of the sulfide grains (an average density of pyrrhotite and pentlandite). As in previous CABMOD studies (Vondrak et al., 2008; Carrillo-Sánchez et al., 2016; Gómez-Martín et al., 2017), isothermal heating of the particles is assumed. While this is valid for homogeneous particles with masses up to 1 mg (Vondrak et al., 2008), it is not supported by empirical observations of actual recovered micrometeorites (Rietmeijer, 1993; Genge et al., 1997; Engrand and Maurette, 1998; Suttle et al., 2019). The heterogeneity of these particles lead to textural features indicating temperature gradients within the (partially) molten particle. However, accounting for chemical gradients and fractionation would add considerable complexity to the model. We also note that the CABMOD models will more accurately simulate anhydrous precursors (CV, CK, CO, OC etc.) rather than hydrated (CM, CI, CR) parent bodies, because thermal gradients are more significant in the hydrated particles. The metallic phase is also assumed to melt homogeneously but not instantaneously. An overview of the algorithm used in CABMOD-3 is depicted as a flowchart (Fig. 1).

The Langmuir evaporation of metallic Fe and Ni is estimated from the vapor pressures compiled in the JANAF thermodynamic tables (Chase et al., 1985). These pressures are applicable to an ideal solution and subsequently need to be corrected by the corresponding Raoultian activity coefficients for a given particle composition and temperature. The relationship between activity a_i and concentration x_i is assumed to be:

$$a_i = \phi_i x_i \tag{4}$$

where ϕ_i is the Raoultian activity coefficient for the species i, i.e. Fe or Ni. Conard et al. (1978) estimated the Raoultian activity coefficients for Fe–Ni alloys in the temperature range 1500 K–1900 K; their results are consistent with recent studies (Cacciamani et al., 2010). These

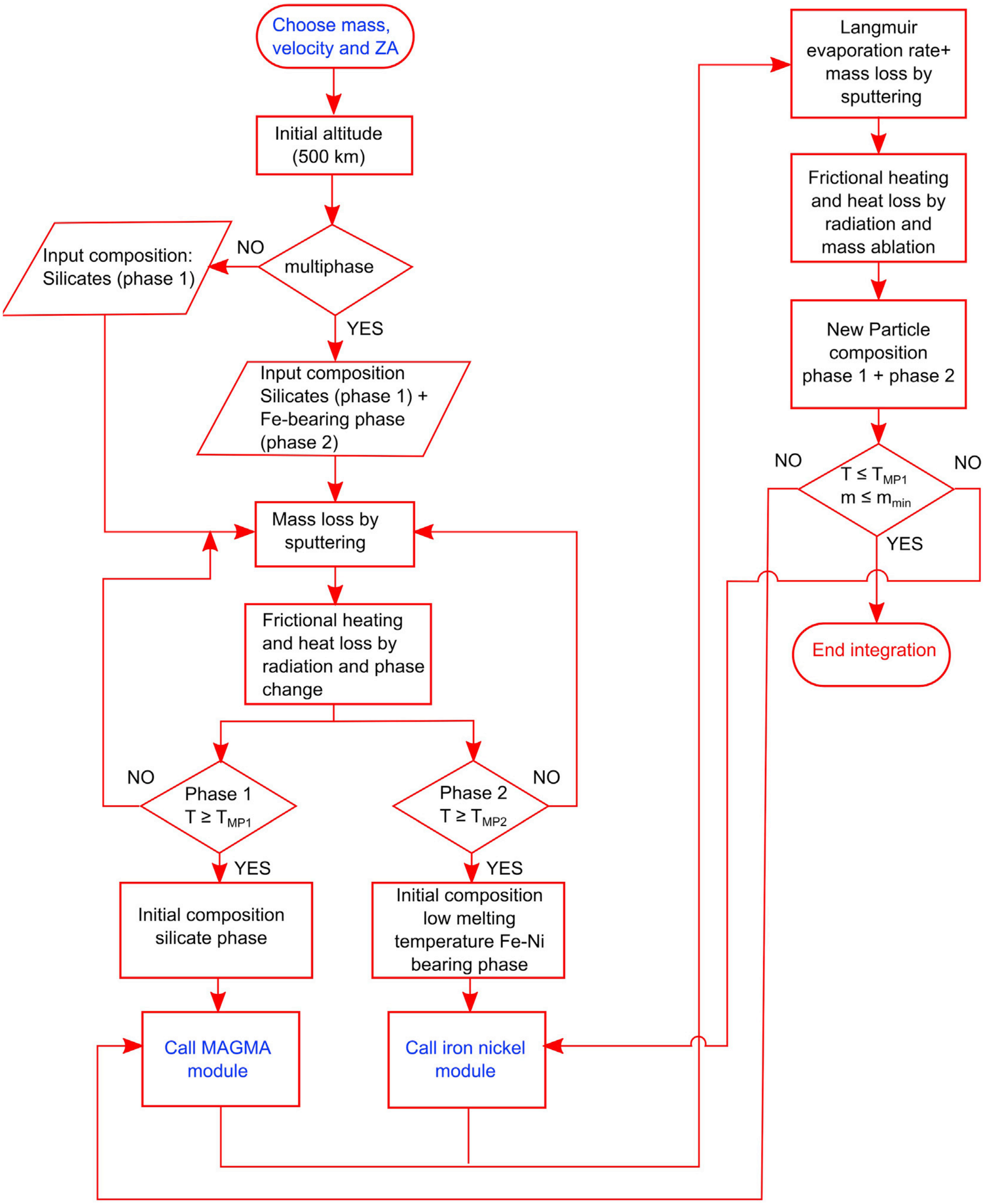

Fig. 1. Flow chart depicting the structure of the multiphase treatment in the Chemical Ablation MODel (CABMOD).

measurements of the thermodynamic properties of the Fe–Ni binary system were extrapolated to 3100 K in order to be used by CABMOD-3. In practice, the metallic phase has largely evaporated before the particle reaches temperatures of 2500 K for all but the largest, fastest particles considered.

Finally, the diffusion of Ni from the particle bulk to the surface is assumed to be rate-limiting for its evaporation. The fraction of Ni diffused in a time interval Δt is given by the solution of the diffusion equation for spherical symmetry (Crank, 1975):

$$f(\Delta t, T) = \frac{6}{\pi^2}\sum_{n=1}^{\infty}\frac{1}{n^2}exp\left(-D^{Ni}(T)n^2\pi^2\frac{\Delta t}{r^2}\right) \tag{5}$$

where $D^{Ni}(T)$ is the diffusion coefficient of Ni at temperature T and is given by the expression:

$$D^{Ni}(T) = D_0^{Ni}exp\left(E_A^{Ni}/RT\right) \tag{6}$$

where the activation energy E_A^{Ni} for Ni is 193 ± 10 kJ mol^{-1} and the pre-exponential factor D_0^{Ni} is 1.1×10^{-9} m^2 s^{-1} (Clark and Long, 1971), resulting in $D^{Ni}(T) = 4.4 \times 10^{-4}$ m^2 s^{-1}. Most recently, Petry et al. (2004) concluded that Ni diffusion in olivine increases with oxygen fugacity. Although their results match very well with Clark and Long (1971) when oxygen fugacity is 10^{-6} Pa, for the higher fugacities present in the molten particle the agreement is less good, leading to a probable underestimate of diffusion.

As CABMOD-3 iterates, the metal and the silicate phases are treated separately except when the momentum/thermal energy balance of the particle is calculated, when the particle is treated as one body. If τ, the width of the phase transition factor, is set to 51 K, then at a temperature of about 230 K below the melting point, the phase transition factor = 0.01 and the phase is 1% melted. The melting temperatures of the metallic phase have been estimated from the phase diagram for Fe–Ni alloy (Bowen and Schairer, 1935; Swartzendruber et al., 1991). This results in melting temperatures of 1760 K for a CI chondrite, 1720 K for Allende particles and 1800 K for Chergach particles.

3. Results

3.1. SEM-EDX analyses

The meteorite and pentlandite samples were analysed by SEM-EDX in order to check that our samples were representative of previous measurements for the bulk abundances in the case of Allende and to ascertain the distribution of minerals within the ground samples, in comparison with an elemental map of an unground sample of Allende.

3.1.1. Allende

A sample of particles from the CV3 meteorite Allende, of average radius 36 μm, was analysed by SEM-EDX (Fig. 2; see Table 1 and Fig. S1 in the Supplementary Material for data on all the detected elements). Ni was present in 4 out of 14 spots analysed, at an average composition of 4 wt% in the 4 spots, or 1.1 wt% overall. Ni is distributed inhomogeneously throughout the particles, often occurring where S is also present. Regions of high atomic weight, such as metal and sulfide phases appear bright in backscattered images (panel a). The elemental abundances measured were consistent with earlier measurements of Allende (Clarke et al., 1970), although the Ni abundance is notably higher than we reported previously from inductively-coupled plasma atomic emission spectroscopy (ICP-AES) measurements (Gómez-Martín et al., 2017; James et al., 2017).

One almost pure particle of Fe–Ni–S is evident in Fig. 2, but the majority are composed mainly of silicate material such as olivine. Fe is present throughout, although concentrated where Ni and S are also present. Ni is also apparent at low levels in the Fe rich regions of the olivine matrix. Elements other than those depicted in Fig. 2 are also present, such as O, Mg, Al and Ca (in decreasing order of abundance). None of these elements are systematically associated here with S or Ni. As we have noted before, Fe abundance tends to vary inversely with respect to Mg in the silicate phase (Bones et al., 2018).

A larger piece of Allende was also analysed (Fig. 3; see Table 1 and Fig. S2 for data on all detected elements). As in the ground-up sample, S rich regions are closely associated with Ni rich regions. Near the middle of the image is an example of a Ni grain almost surrounded by Fe sulfide. The Ni rich grains are typically <5 μm in radius. These observations are consistent with earlier TEM analyses of Allende (Brearley, 1999). The elemental composition was consistent with the particle-by-particle analysis, considering that the particles are highly inhomogeneous. This is clear if the “Allende particles” column is compared with the “Allende

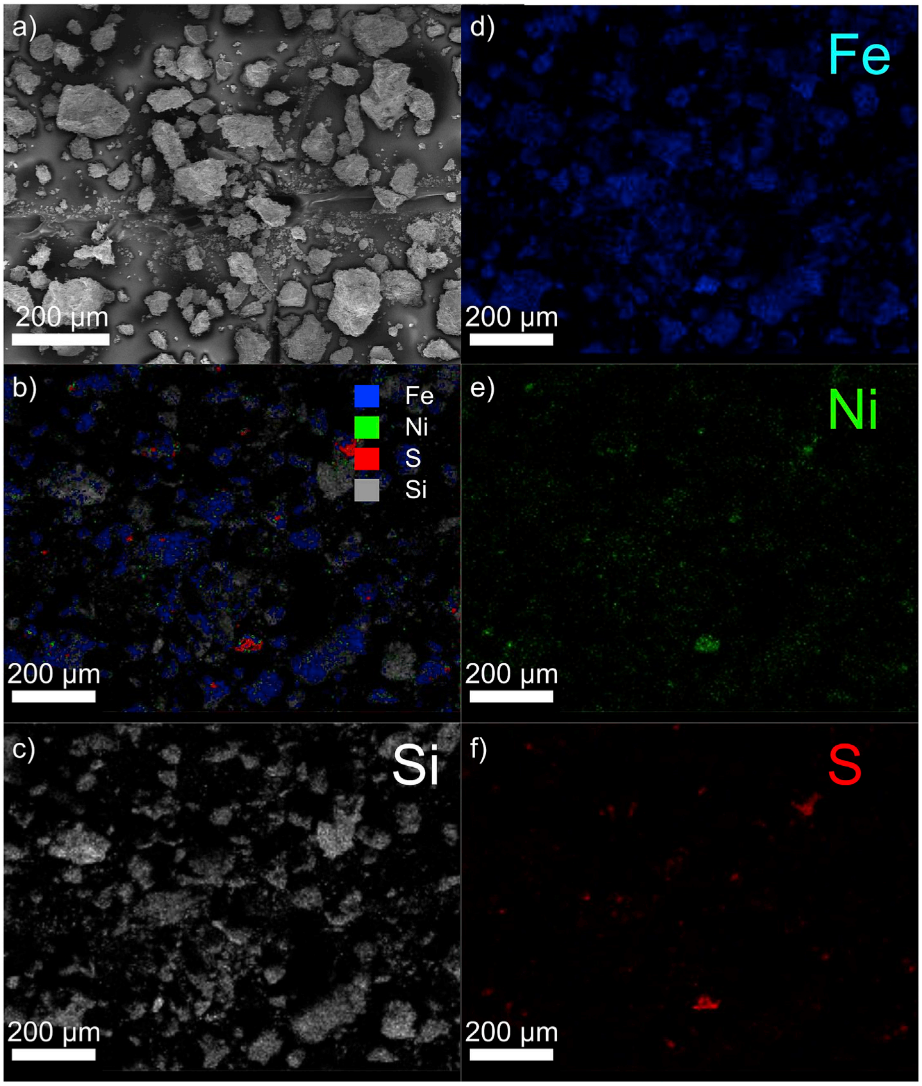

Fig. 2. Allende meteorite particles: a) SEM micrograph of uncoated Allende meteorite particles; b) composite SEM-EDX map; c)-f) Individual SEM-EDX element map for Si, Fe, Ni and S respectively. Plots are available in colour in the online version.

Table 1
Atomic abundances (mol) relative to Si for Allende samples, and the CI and CV chondritic averages (n.d. = not detected).

Element	Allende fragment	Allende particles	Allende particles[a]	Allende bulk[b]	CI average[c]	CV average[c]
	This study	This study				
Mg	0.81 ± 0.21	1.1 ± 0.8	0.61	1.07	1.03	1.05
Fe	0.67 ± 0.24	2.2 ± 2.2	0.44	0.749	0.87	0.753
Al	0.20 ± 0.08	0.09 ± 0.09	0.08	0.112	0.0827	0.111
Ca	0.16 ± 0.06	0.2 ± 0.2	0.04	0.081	0.0604	0.082
S	0.13 ± 0.04′	0.1 ± 0.1	n.d.	0.111	0.0448	0.122
Ni	0.043 ± 0.015	0.2 ± 0.2	0.0007	0.041	0.0483	0.040
Cr	n.d.	0.07 ± 0.07	n.d.	0.036	0.0133	0.012

[a] James et al. (2017).
[b] Clarke et al. (1970).
[c] Lodders and Fegley (2011).

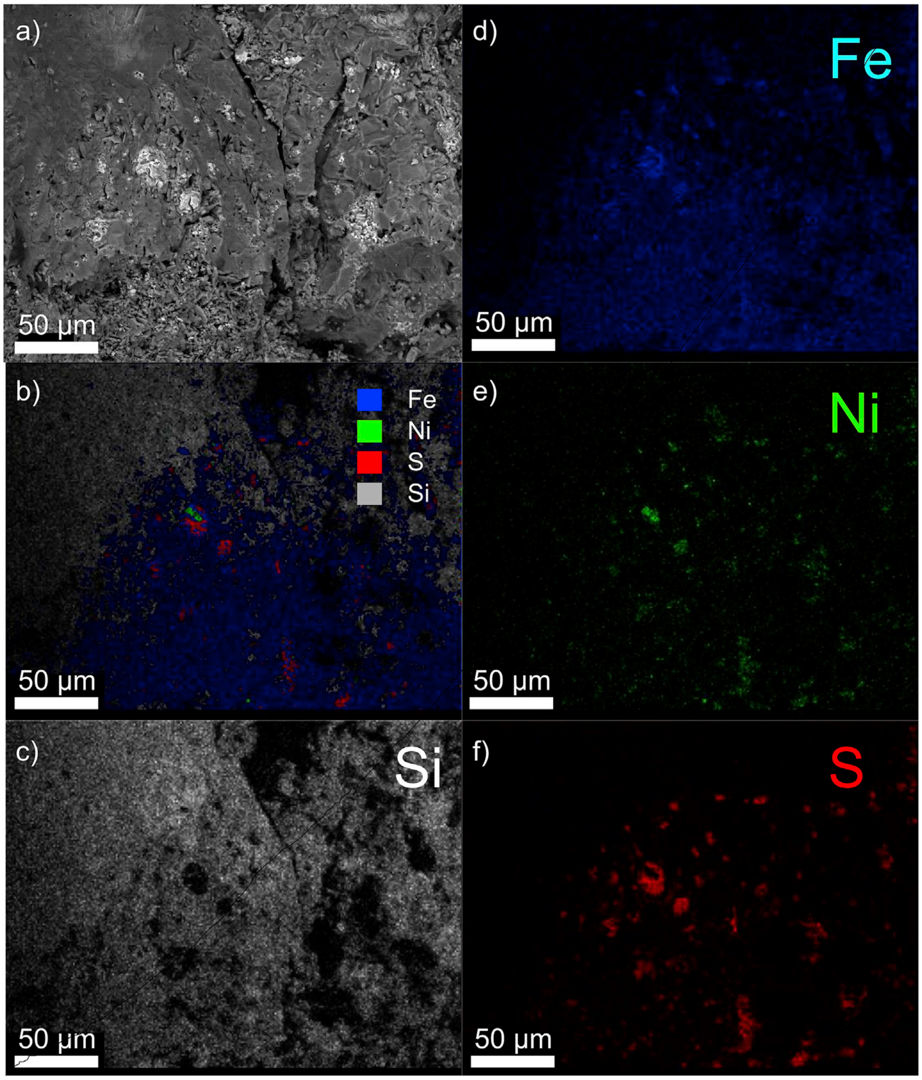

Fig. 3. Solid fragment of the Allende meteorite: a) SEM micrograph of uncoated Allende meteorite piece; b) composite SEM-EDX map; c)-f) Individual SEM-EDX element map for Si, Fe, Ni and S respectively. Plots are available in colour in the online version.

fragment" column in Table 1. The error in the reported ratios, calculated as 1 standard deviation (from 14 spot analyses on the particles), for each element is often as large as the ratio itself. The "Allende piece" results are from 11 EDX maps that mapped different regions each of around 400 by 500 µm of the larger piece of Allende. The uncertainties are much lower than those calculated for the particles.

Based on these and previous analyses, the bulk elemental composition of Allende is a reasonable approximation to the chondritic composition that is presumed to describe the composition of the bulk of the micrometeoroids entering the Earth's atmosphere (Schramm et al., 1989; Taylor et al., 2012; Noguchi et al., 2015). The Ni content is similar to the CI Ni content of 1.1%, and also similar to the average CV3 content of 13200 ppm (Lodders and Fegley, 2011). The distribution of Ni in Allende appears typical of a siderophile element: small grains of pentlandite often associated with larger pyrrhotite grains.

3.1.2. *Chergach*

The heterogeneity observed in Allende samples is even more evident in SEM-EDX maps of a polished piece of the Chergach meteorite (Supplementary Material Figs. S3 and S4 and Table S1), where visible, light-reflecting metallic Fe grains are abundant. Our analysis indicates that Ni is present in these grains at around 3% but also occurs in small Ni rich Fe–Ni grains as can be observed in Fig. S4. Previous SEM-EDX analyses of Chergach (Gómez-Martín et al., 2017; James et al., 2017) indicate the total amount of FeS + Fe metal is similar to the amount of FeS in CI chondrites.

3.1.3. *Pentlandite/pyrrhotite*

Pentlandite is an Fe–Ni sulfide with formula $(Fe,Ni)_9S_8$. It is commonly found mixed with pyrrhotite, $Fe_{1-x}S$, where x is between 0 and 0.125. The sample as obtained had veins of pentlandite/pyrrhotite embedded in breccia. The initial pentlandite/pyrrhotite sample was ground then separated twice magnetically. The resulting flakes were between 10 and 400 µm in radius. EDX analysis reveals that many of the flakes had a high Fe and S content, consistent with pyrrhotite (See SI, Fig. S5). These flakes also had a small amount, typically 1%, of Ni present. The Ni was concentrated in points but also distributed at low concentrations evenly throughout the FeS grains. Other grains appeared to be something completely different (phyllosilicates and albite were suggested in an X-ray diffraction (XRD) analysis).

To improve the sample homogeneity, the pentlandite was reground and further purified by magnetic separation. The sample was later confirmed by XRD to be 6% pentlandite and 19% pyrrhotite, that is, around 3% Ni overall. The average particle size was about 30 µm after regrinding.

3.2. *Linear ramps*

3.2.1. *Previous Fe measurements*

Here, we take the previously reported MASI data for Na and Fe ablation from meteoritic particles (Gómez-Martín et al., 2017) and compare the fit between this data and the versions of CABMOD. Samples were heated with slow linear temperature ramps from 1500 to 2700 K over 10 s (120 K s^{-1}). Fig. 4 shows examples of Na and Fe ablation profiles for an average particle size of 64 µm for both MASI experiments and CABMOD simulations, for the two IDP analogues, Allende and Chergach. CABMOD provides reliable evaporation rates for Na, reproducing the onset, the peak, and the width of the profile. In the case of Fe, MASI evaporation profiles are significantly broader than the corresponding Na signal. This is expected, given that Fe profiles are the sum of ablation from the metallic phase and the forsteritic olivine phase.

As discussed above, CABMOD-2 (Gómez-Martín et al., 2017)) is not a multiphase model since it only considers the silicate melt and, as a consequence, fails to reproduce the onset temperature and the broadness of the Fe MASI profile (Fig. 4a and b, grey curves). However, CABMOD-2 can reproduce the onset temperature and the temperature peak corresponding to the high temperature silicate phase, particularly in the case of Chergach (Fig. 4b).

There are also two technical reasons why the MASI results for Fe are broader than those simulated by both CABMOD-2 and 3, which has also been observed for Mg (Bones et al., 2018). The major reason is the heterogeneity of the sample, as evident from Figs. 2 and 3. Additionally, because molten particles move on the filament once the current reaches a certain threshold (the phenomenon of electromigration (Kumar et al., 2014)), the temperature experienced by the particles is lower than that of the centre of the filament where the pyrometer is focussed. This affects more refractory metals like Mg and Ca in particular (See (Bones et al., 2016) and Gómez-Martín et al. (2017) for more details).

When the multiphase treatment is included in CABMOD-3 (dashed red curves in Fig. 4), a marked improvement is seen in the agreement between the model simulation and the experimental data for the Fe profile. CABMOD-3 is able to reproduce successfully the main features of Fe ablation profiles such as the onset temperature, the asymmetry of the peaks and the width of the profiles.

The panels in Fig. 5 show the appearance temperature (the temperature by which 5% of Fe has ablated) and the full width-half maximum (FWHM) for both Chergach and Allende profiles for particles ranging between 9 and 100 µm in radius, as well as the corresponding model results from CABMOD-2 and CABMOD-3. Fig. 5a indicates that the appearance temperatures predicted by CABMOD-2 are more than 200 K higher than the experimental values measured by MASI for meteoric analogues. The predictions of CABMOD-3 exhibit an evident improvement for both analogues, although the Allende predictions are still about 50 K higher than the experimental values. As pointed out by Gómez-Martín et al. (2017), meteoroid aggregates are rather complex structures and may experience an abrupt reduction of the effective surface area of evaporation given the filling of pores and other irregularities with liquid Fe. As a consequence, significant evaporation of Fe in these aggregates may occur well below the median melting point of 1900 K. Fig. 5b illustrates that the experimental FWHM are significantly wider than simulated by CABMOD-2 and CABMOD-3, most likely due to the meteorite heterogeneity and the technical issues mentioned previously. FWHM is used as a measure of peak width in order to have a consistent metric to compare ablation profiles.

The panels in Fig. 5 show the corresponding results for Fe filings of average radius 98 µm and 99% purity. Because the Fe filings are homogeneous, these measurements represent an independent framework to test the prediction of the metal-phase module in CABMOD-3. Fig. 5a reveals that the appearance temperature of the Fe signal in MASI (green star) and CABMOD-3 (red square) are in excellent accord, even though the electromigration effect significantly broadens the FWHM in MASI data (Fig. 5b).

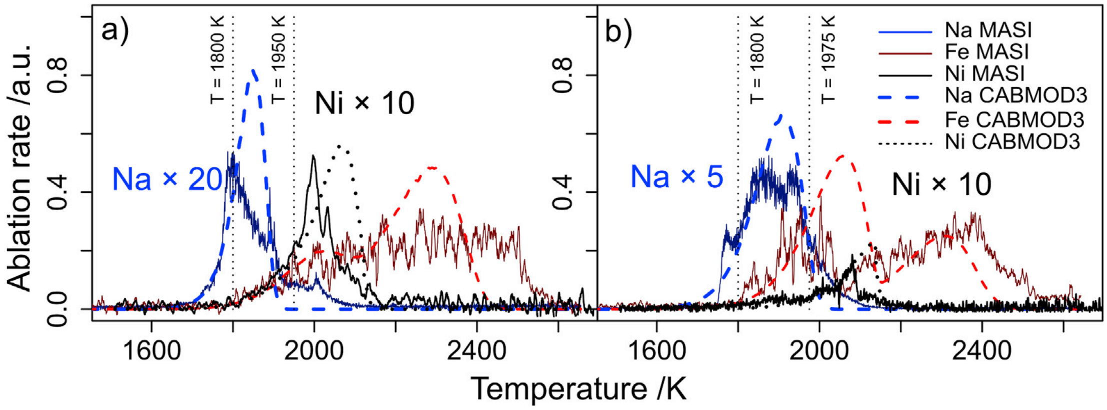

Fig. 4. Normalised LIF profiles from Fe (grey) and Na (orange), compared with model fits for a) Allende and b) Chergach meteorite samples. Plots are available in colour in the online version.

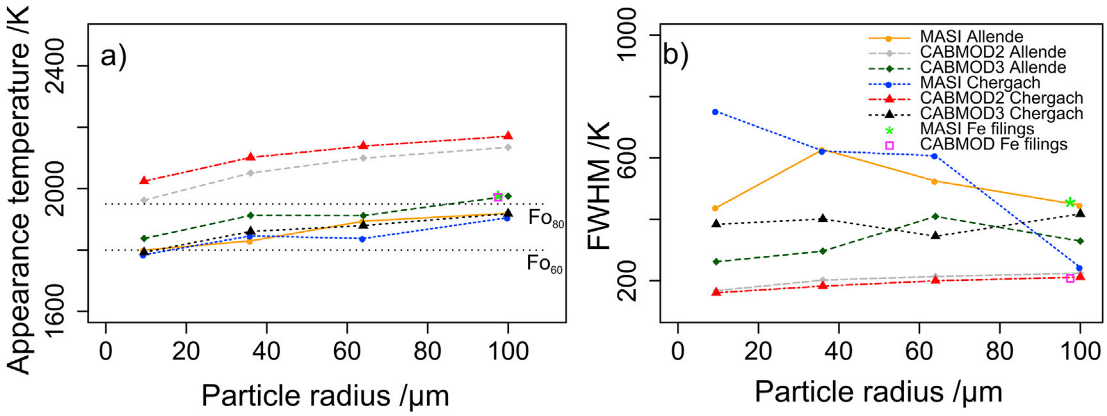

Fig. 5. (a) Appearance temperature: the temperature at which 5% of Fe is ablated; (b) FWHM for Fe ablation curves for meteorite particles between 9 and 100 µm in radius. The horizontal lines in (a) represent the melting temperature of Fo_{60} and Fo_{80}. The solid orange and blue (small dashes) lines are the MASI results for Allende and Chergach. Grey (medium dashes) and red (dash-dot) lines correspond to CABMOD-2 predictions for Allende and Chergach (Gómez-Martín et al., 2017). Green (large dashes) and black (dotted) lines are CABMOD-3 estimates for Allende and Chergach. The green star and red square represent the results from Fe-filings for MASI and CABMOD-3 respectively. Plots are available in colour in the online version. (For interpretation of the references to colour in this figure legend, the reader is referred to the Web version of this article.)

3.2.2. *Ablation of Ni*

In investigations of Ni ablation, the MASI experiment and CABMOD-3 model were also initially tested with simpler sample materials: an Ni–Fe alloy and the mineral pentlandite. As previously, samples were heated with slow linear temperature ramps at 120 K s^{-1}. Fig. 6 displays the resulting Ni signal. Signals are normalised and aligned at their maxima to avoid broadening when the signals are averaged. The averaged signal is displayed as a thick solid line on top of a shaded uncertainty envelope derived from the standard distribution in the individual signals. The CABMOD-3 simulation is the thick dashed line.

Ni–Fe alloy (50:50) powder evaporates at around 2100 K. Once the particle size (radius = 22 µm) was ascertained, CABMOD-3 could reproduce the LIF evaporation profiles with good accuracy. The maximum of the CABMOD-3 profile (dashed line) agrees well with the maximum of the experimental profile. The CABMOD-3 profile is largely within the uncertainty envelope.

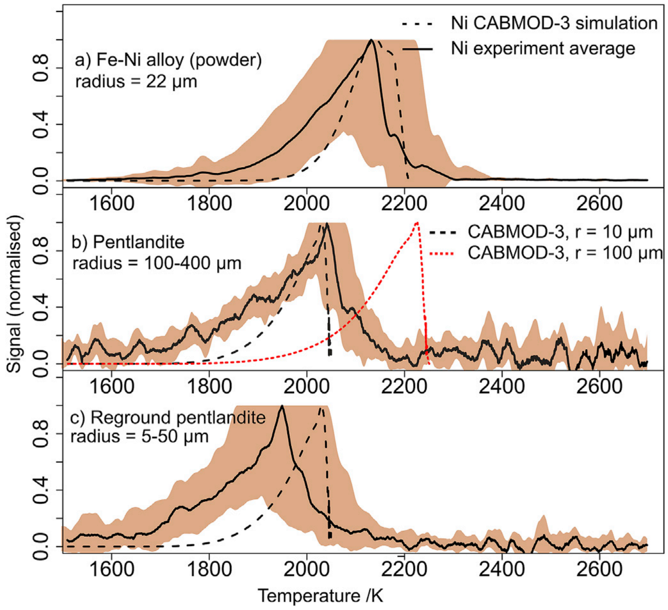

Fig. 6. Normalized Ni LIF profiles resulting from slow linear temperature ramps applied to a) Fe–Ni alloy powder and b), c) pentlandite particles. Thick solid black line: averaged signal. Dashed black line: CABMOD-3 simulation, $r = 10$ µm (dotted red line in middle plot is for $r = 100$ µm particles). The shaded region represents an experimental uncertainty envelope. Plots are available in colour in the online version. (For interpretation of the references to colour in this figure legend, the reader is referred to the Web version of this article.)

The bulk of the Ni in the primary micrometeoroid proxy, the CV3 meteorite Allende, exists largely as NiS or Fe–Ni–S (Li and Agee, 2001; Flores-Gutierrez et al., 2010), consistent with pentlandite, an Fe–Ni sulfide ($(Fe,Ni)_8S_9$). These particles were subjected to the standard linear ramp. Particle sizes varied widely, from about 100 to 400 µm in radius. The particles appeared to be flat plates rather than spheres or cubes. Initial CABMOD-3 simulations produced a poor fit to the experimental Ni signal (Fig. 6, middle plot, red dotted line). However, by reducing the particle size in the simulation to 10 µm, a reasonable fit was obtained both in terms of the temperature where peak signal is observed and in terms of the breadth of the signal (black dashed line). SEM-EDX images of the sample revealed that particles were highly inhomogeneous and tended to have small grains of pentlandite embedded in pyrrhotite (Fe_8S_9) and other (not Ni-containing) minerals with sizes ranging from 5 to 50 µm (Supplementary Material, Fig. S5).

To improve the sample homogeneity, the pentlandite was reground and further purified by magnetic separation. When these particles were heated by the standard linear temperature ramp, the resulting Ni LIF profiles had more spread in temperature of maxima than the original pentlandite sample (Fig. 6 bottom plot). It appears that the regrinding had ground some of the embedded pentlandite grains smaller, along with the breccia matrix, resulting in a greater range of pentlandite grain sizes and greater spread in maximum ablation temperatures.

3.2.3. *Linear ramps with Allende meteorite*

Linear temperature ramps were also applied to meteorite particles as closer proxies for cosmic dust. Particles ground from samples of the Allende meteorite are much closer in composition to cosmic dust than particles from the Chergach meteorite. Both, however are highly heterogeneous and are also subject to a range of heating temperatures on the MASI filament.

As can be seen in Fig. 7, CABMOD-3 is in reasonable agreement with the experimental Ni profiles, although the CABMOD-3 profile consistently shows Ni ablating later than the experimental profile. This suggests that the Ni grains in the Allende particles are small and hence have a large surface area to volume ratio. Hence, they ablate much faster than one large particle of equivalent total volume, which is what CABMOD-3 assumes. This is consistent with the Ni EDX images in Figs. 2e and 3e. Another possibility is that the small grains melt and (being immiscible in the silicate melt) rapidly migrate to the surface, where the low surface tension of Fe–Ni sulfide ensures the metal sulfide melt spreads out over the particle surface and hence ablates rapidly (Taylor et al., 2011). An

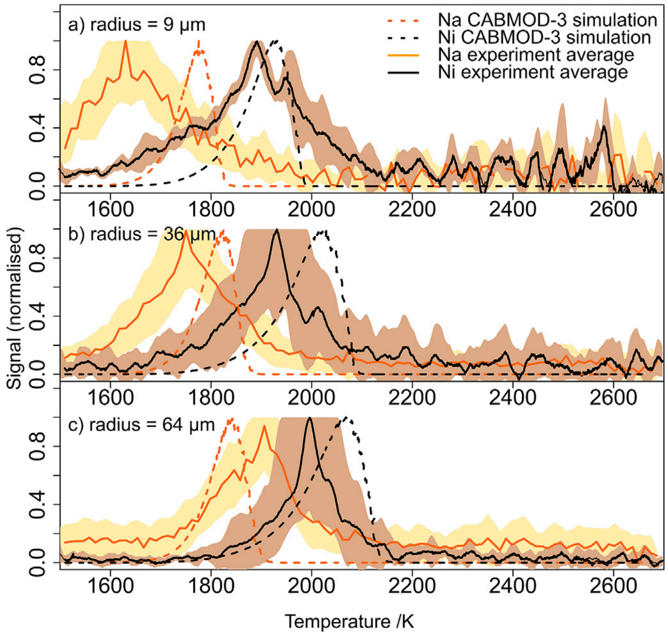

Fig. 7. Normalized Na and Ni LIF profiles resulting from slow linear temperature ramps applied to Allende meteorite particles for 3 different average radii. Thick solid black line: averaged Ni signal. Dashed black line: CABMOD-3 simulation of Ni signal. Thick dash-dot orange line: averaged Na signal. Dotted orange line: CABMOD-3 simulation of Na signal. The brown (dark grey in print version) and yellow (light grey) shaded region represents an experimental uncertainty envelope for Ni and Na profiles, respectively. Plots are available in colour in the online version. (For interpretation of the references to colour in this figure legend, the reader is referred to the Web version of this article.)

alternative explanation to these effects from particle size is that carbothermic reactions such as reaction [1] lead to decomposition of the sulfides and oxides present resulting in evaporation of Ni at temperatures below the expected thermal decomposition temperatures. It is likely that a combination of all of these effects is responsible for the early release of Ni in the experimental runs.

The agreement with the Na profiles (orange lines) is not as good, with the simulated profile from CABMOD-3 peaking between 150 K before, and up to 70 K after, the experimental peak. There is a distinct trend of ablation at higher temperatures for larger radii in the experimental case that is absent in the CABMOD-3 simulations. This is possibly due to the melting point of the particles varying much more than CABMOD-3 assumes. By the time that Ni ablates, the particle has completely melted in all cases. The smallest particles melt and ablate over a broader range of temperatures than larger particles. This smallest size bin would include any particles smaller than 38 µm in diameter (the hole size of the sieve) so could include a substantial fraction of very small particles that melt very quickly.

The differences in composition between the individual particles manifests in the spread of the Na and Ni profiles, in terms of temperatures of ablation and the broadness of individual peaks. This broadening effect is less pronounced in the case of relatively volatile species like Na and Ni than for more refractory metals. Experimental runs generally involved many particles. The smallest size bins required more particles for a measureable signal. Size 1 typically had 100s of particles, whereas size 3 required 5–10.

3.2.4. Linear ramps with Chergach meteorite

The earlier than expected ablation of Na is less apparent for linear ramps applied to particles from the Chergach meteorite (Fig. 8). The SEM-EDX mapping reported here did not detect Na. Previous analyses mapping Na in Chergach particles indicate a heterogeneous distribution, in contrast to the more homogeneous distribution of Allende (Gómez-Martín et al., 2017; James et al., 2017). An explanation could be that Na occurs in larger grains that melt quickly but at higher temperatures.

Chergach is an H5 ordinary chondrite. It has large grains of pure Fe as well as sizeable grains of Fe–Ni. The experimental Ni profiles suggest very little variation in ablation temperature between the different particle sizes. This implies a constant Ni grain size (of radius 7 µm, approximately, based on the good fit between data and model in the particle radius = 36 µm case (panel b)). As mentioned above, CABMOD-3 currently assumes all the metal sulfide phase resides in one mass. However, the SEM-EDX data suggests a large range of Ni grain sizes for both Allende and Chergach (Figs. 2 and 3 and S3). Furthermore, given that meteoroids are an agglomeration of even more primitive minerals, it seems likely the Ni (and Fe and S) grain size would be independent of particle size. It seems likely, then, that there is in fact a bias produced by the meteorite grinding method that results in similar size metal grains.

Frequently, experimental runs with Chergach particles would give no discernible Ni profile even though there were particles visibly present and the Na profile looked normal. When only 5–10 particles are present, as in the experiments with the larger sizes of particles, it was possible to have a sample with no Ni included. This was very rarely seen for Allende samples which have a more homogeneous distribution of Ni grains.

3.3. Atmospheric profiles

Allende and Chergach particles were also subjected to realistic atmospheric temperature profiles. These profiles were simulated by CABMOD-3, taking into account the physical heating of micrometeoroids upon entry into the Earth's atmosphere. Smaller, slower micrometeoroids experience lower peak temperatures and longer duration heating than larger, faster ones (Love and Brownlee, 1991). To a first approximation, the amount of Ni ablation depends largely on the maximum temperature of the profiles.

Fig. 9 depicts atmospheric heating profiles over a range of initial velocities and particle sizes applied to samples from the Allende meteorite (see Supplementary Material, Fig. S6 for the corresponding data from the Chergach meteorite). Particle sizes and velocities were chosen based on the expected size and velocity distributions of particles from Jupiter family comets, at least as far as the thermal profiles could be reproduced within the temperature range of the pyrometer. The evaporation profiles of Na and Ni are overlaid with CABMOD-3 predictions. In general the rate of heating is very fast compared with the linear temperature ramps, up to 1400 K s^{-1}. The evaporation peaks of Na and Ni therefore appear soon after the start of heating and are close together. The rapid heating rate also helps to minimize the spread of ablation temperatures compared with those observed for the linear ramps. In general this is well captured in the CABMOD-3 simulation. The simulated profiles are generally around 80% narrower than the experimental ones, but this difference is less than observed in previous MASI studies of other elements such as Fe and Mg. As observed in the linear ramps, the CABMOD-3 profile peaks slightly after the experimental profile in the majority of cases, again suggesting a larger surface area to volume ratio than accounted for in the model.

Similarly to the linear temperature ramp data, the times of maximum evaporation of the experimental profiles in Fig. 9 are aligned before the average is taken, with uncertainty in time and signal represented by envelopes for each metal. The profiles are normalised to 1 then multiplied by the fraction ablated (for both MASI and CABMOD data). The bar at the top of each plot also represents the experimental fraction of Ni ablated out of the total Ni present in the particle.

Fig. 10 plots the temperature of maximum ablation of Ni versus the maximum temperature experienced by the particle (for particles with Allende composition; see the Supplementary Material Fig. S7 for the corresponding plot for the Chergach meteorite). Particles of the same size but moving at faster velocities undergo maximum ablation of Ni at slightly higher temperatures, according to CABMOD-3 simulations, but in

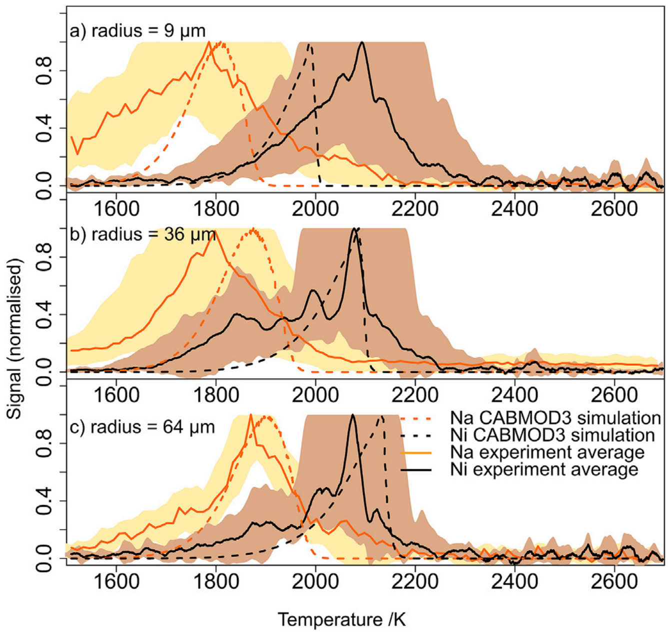

Fig. 8. Normalized Na and Ni LIF profiles resulting from slow linear temperature ramps applied to Chergach meteorite particles for 3 different average radii. Thick solid black line: averaged Ni signal. Dashed black line: CABMOD-3 simulation of Ni signal. Thick dash-dot orange line: averaged Na signal. Dotted orange line: CABMOD-3 simulation of Na signal. The brown (dark grey in print version) and yellow (light grey) shaded region represents an experimental uncertainty envelope for Ni and Na profiles, respectively. Plots are available in colour in the online version. (For interpretation of the references to colour in this figure legend, the reader is referred to the Web version of this article.)

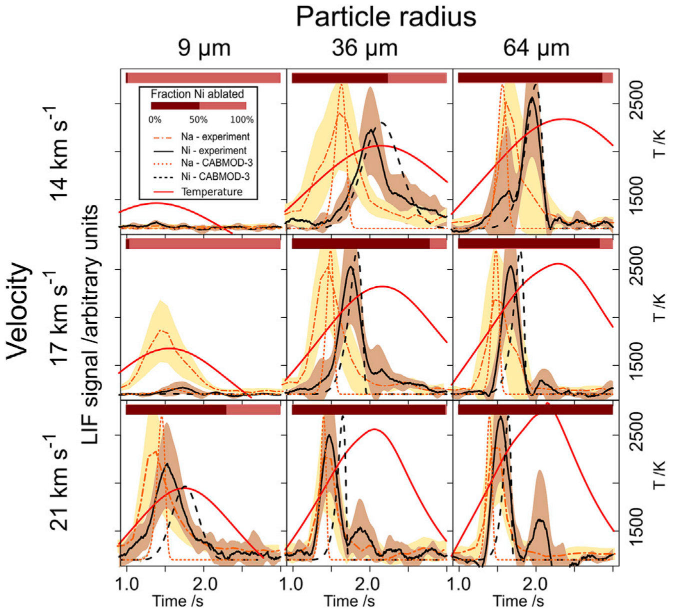

Fig. 9. Normalized Na and Ni LIF profiles resulting from atmospheric temperature profiles applied to Allende meteorite particles, for a range of particle sizes and entry velocities. Thick solid black line: averaged Ni signal. Dashed black line: CABMOD-3 simulation of Ni signal. Thick dash-dot orange line: averaged Na signal. Dotted orange line: CABMOD-3 simulation of Na signal. Solid red line: Temperature. The brown (dark grey) and yellow (light grey) shaded region represents an experimental uncertainty envelope for Ni and Na profiles, respectively. The bar at the top of each plot represents the average experimental fraction ablated for each size/velocity combination. Plots are available in colour in the online version. (For interpretation of the references to colour in this figure legend, the reader is referred to the Web version of this article.)

general the maximum ablation happens at around 2250 K if the particle reaches this temperature. Overall, MASI measurements of the temperature of maximum ablation of Ni are lower than the CABMOD-3 predictions, consistent with the earlier than predicted ablation of Ni, as seen in Fig. 7.

Fig. 11 depicts two examples of atmospheric ablation profiles with experimental and CABMOD-3 results from Allende particles, with altitude on the ordinate axis and with the atomic injection rate on the abscissa. Fe data from earlier measurements (Gómez-Martín et al., 2017) is also included. In both the laboratory MASI simulation of atmospheric entry, and the CABMOD-3 prediction, Ni ablates in a narrow altitude range slightly below Na and before the majority of Fe. CABMOD-3 predictions suggest that all the Ni in a carbonaceous chondrite experiencing temperatures greater than 2400 K will ablate. The experiments indicate a lower threshold of 2200 K for complete ablation. Again, this lower threshold can be largely explained by the small grain sizes present in the actual meteorite samples and potential decomposition of sulfides in carbothermic reactions.

While the altitude of maximum ablation and the relative amounts of ablated metal are well captured by CABMOD-3, the experimental profiles are again much broader than the computer simulation. This is particularly evident for Fe. As mentioned earlier, the combination of meteorite heterogeneity and electromigration results in a broadening of the experimental profiles. These effects are less pronounced for Ni, however, as it ablates early and so tends to avoid effects from particle movement on the filament.

Many small grains would ablate more rapidly than one large grain of equivalent volume, since the rate of evaporation depends on surface area. Therefore, small grains of Fe–Ni–S would be expected to ablate rapidly once they melt. This matches what we see with Allende meteorite samples. In contrast, for micrometeoroids with high Fe–Ni content similar to that of Chergach, the likelihood is that the molten grains would combine as they migrate to the surface (Taylor et al., 2011). FeS has a low surface tension and will spread out to cover the surface of the particle. It is this large surface area that allows for rapid evaporation of first FeS and then FeNi. CABMOD-3 in its current form does not allow for this possibility.

Although Allende has a relatively low metallic Fe–Ni abundance, the improvements in CABMOD-3 make a significant difference to the shape of the simulated Fe ablation profiles. A similar difference would be seen for cosmic dust of CI chondritic composition, given that the metallic Fe–Ni abundance is similar. The ablation of metallic Fe and Ni would also be enhanced if FeO is reduced by the pyrolysis of carbon (see Equation [1]). CI and CM chondrites typically have C at abundances of around 2% (Lodders and Fegley, 2011).

3.4. *Differential ablation comparisons*

In previous papers we have used the Differential Ablation Coefficient (DAC) as a metric to compare the ablation of meteoric metals in the MASI experiments with CABMOD-2 simulations. The DAC is the fraction of an element ablated (Φ_M), relative to Na, multiplied by its abundance n_M, relative to Na:

$$DAC = \frac{\Phi_M}{\Phi_{Na}} \frac{n_M}{n_{Na}}$$

Here, we focus on the fraction of Ni and Na ablated as a more intuitive measure of ablation.

Micrometeoroids enter the atmosphere with a range of particle sizes and velocities. The fractions ablated in Table 2 are averaged over the sizes and velocities used in the experimental MASI runs, weighted to account for the actual size and velocity distributions of dust from cometary and asteroidal sources. See Carrillo-Sánchez et al. (2016) for more details of these distributions or Bones et al. (2018) and Gómez-Martín et al. (2017) for examples for other elements.

The CABMOD-3 simulations were run for the same set of particle sizes

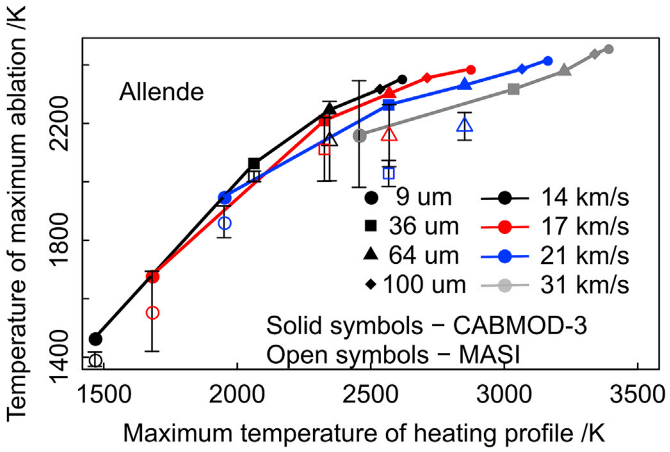

Fig. 10. The temperature of maximum ablation of Ni plotted as a function of overall maximum temperature, for 4 different Allende meteorite particle sizes and four different velocities, for CABMOD-3 simulations and MASI data (see Figure legend). Plots are available in colour in the online version.

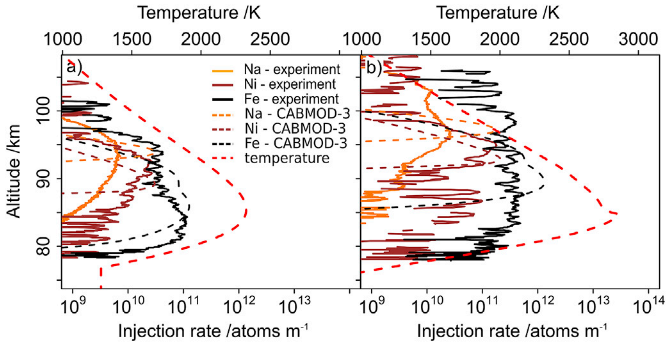

Fig. 11. Normalized ablation profiles as a function of altitude (vertical axis). a) Allende meteorite, 17 km s^{-1}, 36 μm particles. b) Allende meteorite, 21 km s^{-1}, 64 μm particles. Solid lines: Averaged MASI signal, normalized to the DAC (see Section 3.4). Dashed lines: CABMOD-3 predictions. Na: orange (light grey in print version); Ni: brown (dark grey); Fe: Black. Temperature profile: red dashed line. Plots are available in colour in the online version. (For interpretation of the references to colour in this figure legend, the reader is referred to the Web version of this article.)

Table 2
Fraction ablated during MASI experiments and CABMOD-3 simulations (n.m. = not measured).

Simulation	Meteorite	Na	Ni	Fe[a]
MASI	Allende	0.62 ± 0.19	0.46 ± 0.14	0.32 ± 0.06
CABMOD-3	Allende	0.59	0.49	0.30
MASI	Chergach	0.55 ± 0.22	0.37 ± 0.19	n.m.
CABMOD-3	Chergach	0.62	0.57	0.49

[a] Experimental data for Fe from Gómez-Martín et al. (2017). CABMOD simulations are from CABMOD-3. The corresponding values for CABMOD-2 are 0.27 (Allende) and 0.32 (Chergach).

and velocities, allowing a direct comparison with the MASI results. The agreement in Table 2 is very good (apart from Chergach Ni which is just outside the limit of the MASI uncertainty).

4. Conclusions

The MASI experimental setup has been used to test the CABMOD-3 simulation of Ni ablation over slow linear temperature ramps and realistic atmospheric temperature profiles. In the absence of genuine pristine micrometeoroids, samples of powdered terrestrial meteorites serve as informative proxies as long as compositional differences between the meteorites and the interplanetary micrometeoroid population are understood. The mostly good agreement between CABMOD-3 simulations and MASI experiments gives us confidence in the ability of CABMOD-3 to simulate the ablation of metals from micrometeoroids entering the atmospheres of Earth and other planets. Typically the experimental data suggests that Ni ablates at lower temperatures than predicted by CABMOD-3. The reason is evident from the linear temperature ramp experiments: these experiments underline the importance of accurately representing Ni grain size to get the best prediction of Ni ablation as a function of altitude.

Both MASI data and CABMOD-3 simulations agree that the ablation of Ni (and by extension, metallic or sulfide Fe) occurs rapidly and at the relatively low temperature of around 2200 K, before the bulk of the silicate Fe has ablated, as previously reported by Taylor et al. (2011). Ni is also seen to ablate completely for a wider range of particle sizes and velocities than Fe in both experiment and simulation. This may help to explain the observed depletion of Ni in micrometeorites (Kurat et al., 1994; Taylor et al., 2000).

In a subsequent paper the impact of micrometeoroids on different planetary atmospheres will be examined. Simulations will be conducted using CABMOD-3 to compare the Meteoric Input Function (MIF) for Fe, Ni and other elements for Earth, Mars and Venus (Carrillo-Sánchez et al., 2020).

Acknowledgements

This work was supported by the UK Natural Environment Research Council (grant number NE/P001815/1). The raw MASI ablation data and CABMOD output are available from the Centre for Environmental Data Analysis (CEDA) archive (doi for MASI data:10.5285/8120f50827564bd7ae22ee3ac50e6c8f; doi for CABMOD data:10.5285/5f7c65c06317418f8ff0b6881c929153). SEM images and analysis scripts and Excel spreadsheets are archived at the University of Leeds, doi:10.5518/714.

Appendix A. Supplementary data

Supplementary data to this article can be found online at https://doi.org/10.1016/j.pss.2019.104725.

References

Alexander, C.M.O., Taylor, S., Delaney, J.S., Peixue, M., Herzog, G.F., 2002. Mass-dependent fractionation of Mg, Si, and Fe isotopes in five stony cosmic spherules. Geochem. Cosmochim. Acta 66, 173–183.

Bones, D.L., Gómez-Martin, J.C., Empson, C.J., Carrillo-Sánchez, J.D., James, A.D., Conroy, T.P., Plane, J.M.C., 2016. A novel instrument to measure differential ablation of meteorite samples and proxies: the Meteoric Ablation Simulator (MASI). Rev. Sci. Instrum. 87, 12. https://doi.org/10.1063/1.4962751.

Bones, D.L., Gómez Martín, J.C., Carrillo Sánchez, J.D., Dobson, A.J., Plane, J.M.C., 2018. Characterization of the extraterrestrial magnesium source in the atmosphere using a meteoric ablation simulator. Geophys. Res. Lett. 45 https://doi.org/10.1029/2018GL077427.

Bowen, N.L., Schairer, J.F., 1935. The system, MgO-FeO-SiO2. Am. J. Sci. 29, 151–217.

Brearley, A.J., 1999. Origin of graphitic carbon and pentlandite in matrix olivines in the Allende meteorite. Science 285, 1380–1382. https://doi.org/10.1126/science.285.5432.1380.

Cacciamani, G., Dinsdale, A., Palumbo, M., Pasturel, A., 2010. The Fe-Ni system: thermodynamic modelling assisted by atomistic calculations. Intermetallics 18, 1148–1162. https://doi.org/10.1016/j.intermet.2010.02.026.

Carrillo-Sánchez, J.D., Gómez-Martín, J.C., Bones, D.L., Nesvorný, D., Pokorný, P., Benna, M., Plane, J.M.C., 2020. Cosmic dust flux in the atmospheres of Earth, Mars, and Venus. Icarus 335, 113395. https://doi.org/10.1016/j.icarus.2019.113395. In press.

Carrillo-Sánchez, J.D., Nesvorný, D., Pokorný, P., Janches, D., Plane, J.M.C., 2016. Sources of cosmic dust in the Earth's atmosphere. Geophys. Res. Lett. 43 (11) https://doi.org/10.1002/2016GL071697, 979-911,986.

Chase, M.W., Davies, C.A., Downey Jr., J.R., Frurip, D.J., McDonald, R.A., Syverud, A.N., 1985. JANAF thermodynamic tables. J. Phys. Chem. Ref. Data 14 (1), 1174–1179.

Clark, A.M., Long, J.V.P., 1971. The anisotropic diffusion of nickel in olivine. Gordon and Breach, New York.

Clarke, R.S.J., Jarosewich, E., Mason, B., Nelen, J., Gómez, M., Hyde, J.R., 1970. The Allende, Mexico, meteorite shower. Smithson. Contrib. Earth Sci. 5.

Collins, R.L., Li, J., Martus, C.M., 2015. First lidar observation of the mesospheric nickel layer. Geophys. Res. Lett. 42, 665–671. https://doi.org/10.1002/2014gl062716.

Conard, B.R., McAneney, T.B., Sridhar, R., 1978. Thermodynamics of iron-nickel alloys by mass spectrometry. Metall. Trans. B Process Metall. 9, 463–468. https://doi.org/10.1007/bf02654422.

Consolmagno, G.J., Britt, D.T., Macke, R.J., 2008. The significance of meteorite density and porosity. Chem. Erde Geochem. 68, 1–29. https://doi.org/10.1016/j.chemer.2008.01.003.

Cordier, C., van Ginneken, M., Folco, L., 2011. Nickel abundance in stony cosmic spherules: constraining precursor material and formation mechanisms. Meteorit. Planet. Sci. 46, 1110–1132. https://doi.org/10.1111/j.1945-5100.2011.01218.x.

Court, R.W., Tan, J., 2016. Insights into secondary reactions occurring during atmospheric ablation of micrometeoroids. Meteorit. Planet. Sci. 51, 1163–1183. https://doi.org/10.1111/maps.12652.

Crank, J., 1975. The Mathematics of Diffusion. Clarendon Press, Oxford.

Dobrica, E., Engrand, C., Leroux, H., Rouzaud, J.N., Duprat, J., 2012. Transmission electron microscopy of CONCORDIA UltraCarbonaceous antarctic MicroMeteorites (UCAMMs): mineralogical properties. Geochem. Cosmochim. Acta 76, 68–82. https://doi.org/10.1016/j.gca.2011.10.025.

Engrand, C., Maurette, M., 1998. Carbonaceous micrometeorites from Antarctica. Meteorit. Planet. Sci. 33, 565–580. https://doi.org/10.1111/j.1945-5100.1998.tb01665.x.

Fegley, B., Cameron, A.G.W., 1987. A vaporization model for iron silicate fractionation in the Mercury protoplanet. Earth Planet. Sci. Lett. 82, 207–222. https://doi.org/10.1016/0012-821x(87)90196-8.

Feng, W., Marsh, D.R., Chipperfield, M.P., Janches, D., Hoffner, J., Yi, F., Plane, J.M.C., 2013. A global atmospheric model of meteoric iron. J. Geophys. Res. Atmos. 118, 9456–9474. https://doi.org/10.1002/jgrd.50708.

Flores-Gutierrez, D., Urrutia-Fucugauchi, J., Perez-Cruz, L., Diaz-Hernandez, R., Linares-Lopez, C., 2010. Scanning electron microscopy characterization of iron, nickel and sulfur in chondrules from the Allende meteorite - further evidence for between-chondrules major compositional differences. Rev. Mex. Ciencias Geol. 27, 338–346.

Fredriksson, K., Kerridge, J.F., 1988. Carbonates and sulfates in CI chondrites - formation by aqueous acitivity on the parent body. Meteoritics 23, 35–44. https://doi.org/10.1111/j.1945-5100.1988.tb00894.x.

Genge, M.J., Grady, M.M., Hutchison, R., 1997. The textures and compositions of fine-grained Antarctic micrometeorites: implications for comparisons with meteorites. Geochem. Cosmochim. Acta 61, 5149–5162. https://doi.org/10.1016/s0016-7037(97)00308-6.

Genge, M.J., Grady, M.M., 1998. Melted micrometeorites from Antarctic ice with evidence for the separation of immiscible Fe-Ni-S liquids during entry heating. Meteorit. Planet. Sci. 33, 425–434. https://doi.org/10.1111/j.1945-5100.1998.tb01647.x.

Genge, M.J., Engrand, C., Gounelle, M., Taylor, S., 2008. The classification of micrometeorites. Meteorit. Planet. Sci. 43, 497–515. https://doi.org/10.1111/j.1945-5100.2008.tb00668.x.

Gerding, M., Daly, S.M., Plane, J.M.C., 2018. Lidar soundings of the mesospheric nickel layer using Ni(^{3}F) and Ni(^{3}D) transitions. Geophys. Res. Lett. 46, 408–415.

Gómez-Martín, J.C., Bones, D.L., Carrillo-Sánchez, J.D., James, A.D., Trigo-Rodriguez, J.M., Fegley, B., Plane, J.M.C., 2017. Novel experimental simulations of the atmospheric injection of meteoric metals. Astrophys. J. 836 https://doi.org/10.3847/1538-4357/aa5c8f art. no. 212.

Grady, M.M., Pratesi, G., Moggi Cecchi, V., 2014. Atlas of Meteorites. Cambridge University Press, Cambridge, UK.

Hilchenbach, M., Kissel, J., Langevin, Y., Briois, C., von Hoerner, H., Koch, A., Schulz, R., Silen, J., Altwegg, K., Colangeli, L., Cottin, H., Engrand, C., Fischer, H., Glasmachers, A., Grun, E., Haerendel, G., Henkel, H., Hofner, H., Hornung, K., Jessberger, E.K., Lehto, H., Lehto, K., Raulin, F., Le Roy, L., Ryno, J., Steiger, W., Stephan, T., Thirkell, L., Thomas, R., Torkar, K., Varmuza, K., Wanczek, K.P., Altobelli, N., Baklouti, D., Bardyn, A., Fray, N., Kruger, H., Ligier, N., Lin, Z., Martin, P., Merouane, S., Orthous-Daunay, F.R., Paquette, J., Revillet, C., Siljestrom, S., Stenzel, O., Zaprudin, B., 2016. Comet 67p/churyumov-gerasimenko: close-up on dust particle fragments. Astrophys. J. Lett. 816 https://doi.org/10.3847/2041-8205/816/2/l32.

James, A.D., Frankland, V.L.F., Trigo-Rodríguez, J.M., Alonso-Azcárate, J., Gómez Martín, J.C., Plane, J.M.C., 2017. Synthesis and characterisation of analogues for interplanetary dust and meteoric smoke particles. J. Atmos. Sol. Terr. Phys. 162, 178–191.

Kumar, P., Howarth, J., Dutta, I., 2014. Electric current induced flow of liquid metals: mechanism and substrate-surface effects. J. Appl. Phys. 115, 044915 https://doi.org/10.1063/1.4863641 art. no.

Kurat, G., Koeberl, C., Presper, T., Brandstatter, F., Maurette, M., 1994. Petrology and geochemistry of antarctic micrometeorites. Geochem. Cosmochim. Acta 58, 3879–3904. https://doi.org/10.1016/0016-7037(94)90369-7.

Levasseur-Regourd, A.-C., Agarwal, J., Cottin, H., Engrand, C., Flynn, G., Fulle, M., Gombosi, T., Langevin, Y., Lasue, J., Mannel, T., Merouane, S., Poch, O., Thomas, N., Westphal, A., 2018. Cometary dust. Space Sci. Rev. 214 https://doi.org/10.1007/s11214-018-0496-3.

Li, J., Agee, C.B., 2001. The effect of pressure, temperature, oxygen fugacity and composition on partitioning of nickel and cobalt between liquid Fe-Ni-S alloy and liquid silicate: implications for the Earth's core formation. Geochem. Cosmochim. Acta 65, 1821–1832. https://doi.org/10.1016/s0016-7037(00)00613-x.

Lodders, K., Fegley, B.J., 2011. Chemistry of the Solar System. The Royal Society of Chemistry, Cambridge, UK.

Love, S.G., Brownlee, D.E., 1991. Heating and thermal transformation of micrometeroids entering the earths atmosphere. Icarus 89, 26–43. https://doi.org/10.1016/0019-1035(91)90085-8.

Nesvorny, D., Jenniskens, P., Levison, H.F., Bottke, W.F., Vokrouhlicky, D., Gounelle, M., 2010. Cometary origin of the zodiacal cloud and carbonaceous micrometeorites. Implications for hot debris disks. Astrophys. J. 713, 816–836. https://doi.org/10.1088/0004-637x/713/2/816.

Noguchi, T., Ohashi, N., Tsujimoto, S., Mitsunari, T., Bradley, J.P., Nakamura, T., Toh, S., Stephan, T., Iwata, N., Imae, N., 2015. Cometary dust in Antarctic ice and snow: past and present chondritic porous micrometeorites preserved on the Earth's surface. Earth Planet. Sci. Lett. 410, 1–11. https://doi.org/10.1016/j.epsl.2014.11.012.

Noguchi, T., Yabuta, H., Itoh, S., Sakamoto, N., Mitsunari, T., Okubo, A., Okazaki, R., Nakamura, T., Tachibana, S., Terada, K., Ebihara, M., Imae, N., Kimura, M., Nagahara, H., 2017. Variation of mineralogy and organic material during the early stages of aqueous activity recorded in Antarctic micrometeorites. Geochem. Cosmochim. Acta 208, 119–144. https://doi.org/10.1016/j.gca.2017.03.034.

Pavlov, A.V., 2012. Ion chemistry of the ionosphere at E- and F-region altitudes: a review. Surv. Geophys. 33, 1133–1172. https://doi.org/10.1007/s10712-012-9189-8.

Petry, C., Chakraborty, S., Palme, H., 2004. Experimental determination of Ni diffusion coefficients in olivine and their dependence on temperature, composition, oxygen fugacity, and crystallographic orientation. Geochem. Cosmochim. Acta 68, 4179–4188. https://doi.org/10.1016/j.gca.2004.02.024.

Plane, J.M.C., 2003. Atmospheric chemistry of meteoric metals. Chem. Rev. 103, 4963–4984. https://doi.org/10.1021/cr0205309.

Plane, J.M.C., Feng, W., Dawkins, E.C.M., 2015. The mesosphere and metals: chemistry and changes. Chem. Rev. 115, 4497–4541. https://doi.org/10.1021/cr500501m.

Rietmeijer, F.J.M., 1993. Micrometeorite dynamic pyrometamorphism: observation of a thermal gradient in iron-nickel sulfide. Lunar Planet. Sci. Conf. 24.

Sanloup, C., Fei, Y., 2004. Closure of the Fe-S-Si liquid miscibility gap at high pressure. Phys. Earth Planet. Inter. 147, 57–65. https://doi.org/10.1016/j.pepi.2004.06.008.

Schaefer, L., Fegley, B., 2005. Application of an equilibrium vaporization model to the ablation of chondritic and achondritic meteoroids. Earth Moon Planets 95, 413–423. https://doi.org/10.1007/s11038-005-9030-1.

Schramm, L.S., Brownlee, D.E., Wheelock, M.M., 1989. Major element composition of stratospheric micrometeorites. Meteoritics 24, 99–112. https://doi.org/10.1111/j.1945-5100.1989.tb00950.x.

Stenzel, O.J., Hilchenbach, M., Merouane, S., Paquette, J., Varmuza, K., Engrand, C., Brandstätter, F., Koeberl, C., Ferrière, L., Filzmoser, P., Siljeström, S., the, C.t., 2017. Similarities in element content between comet 67P/Churyumov–Gerasimenko coma dust and selected meteorite samples. Mon. Not. R. Astron. Soc. 469, S492–S505. https://doi.org/10.1093/mnras/stx1908.

Suttle, M.D., Genge, M.J., Folco, L., Van Ginneken, M., Lin, Q., Russell, S.S., Najorka, J., 2019. The atmospheric entry of fine-grained micrometeorites: the role of volatile gases in heating and fragmentation. Meteorit. Planet. Sci. 54, 503–520. https://doi.org/10.1111/maps.13220.

Swartzendruber, L.J., Itkin, V.P., Alcock, C.B., 1991. The Fe-Ni (iron-nickel) system. J. Phase Equilibria 12, 288–312. https://doi.org/10.1007/bf02649918.

Taylor, S., Lever, J.H., Harvey, R.P., 2000. Numbers, types, and compositions of an unbiased collection of cosmic spherules. Meteorit. Planet. Sci. 35, 651–666. https://doi.org/10.1111/j.1945-5100.2000.tb01450.x.

Taylor, S., Jones, K.W., Herzog, G.F., Hornig, C.E., 2011. Tomography: a window on the role of sulfur in the structure of micrometeorites. Meteorit. Planet. Sci. 46, 1498–1509. https://doi.org/10.1111/j.1945-5100.2011.01245.x.

Taylor, S., Matrajt, G., Guan, Y.B., 2012. Fine-grained precursors dominate the micrometeorite flux. Meteorit. Planet. Sci. 47, 550–564. https://doi.org/10.1111/j.1945-5100.2011.01292.x.

Tielens, A.G.G.M., McKee, C.F., Seab, C.G., Hollenbach, D.J., 1994. The physics of grain-grain collisions and gas-grain sputtering in interstellar shocks. Astrophys. J. 431, 321–340. https://doi.org/10.1086/174488.

Vondrak, T., Plane, J.M.C., Broadley, S., Janches, D., 2008. A chemical model of meteoric ablation. Atmos. Chem. Phys. 8, 7015–7031.

Walder, P., Pelton, A.D., 2005. Thermodynamic modeling of the Fe-S system. J. Phase Equilibria Diffusion 26, 23.

Wilms, H., Rapp, M., Kirsch, A., 2016. Nucleation of mesospheric cloud particles: sensitivities and limits. J. Geophys. Res. A Space Phys. 121, 2621–2644. https://doi.org/10.1002/2015ja021764.

Zolensky, M.E., Zega, T.J., Yano, H., Wirick, S., Westphal, A.J., Weisberg, M.K., Weber, I., Warren, J.L., Velbel, M.A., Tsuchiyama, A., Tsou, P., Toppani, A., Tomioka, N., Tomeoka, K., Teslich, N., Taheri, M., Susini, J., Stroud, R., Stephan, T., Stadermann, F.J., Snead, C.J., Simon, S.B., Simionovici, A., See, T.H., Robert, F., Rietmeijer, F.J.M., Rao, W., Perronnet, M.C., Papanastassiou, D.A., Okudaira, K., Ohsumi, K., Ohnishi, I., Nakamura-Messenger, K., Nakamura, T., Mostefaoui, S., Mikouchi, T., Meibom, A., Matrajt, G., Marcus, M.A., Leroux, H., Lemelle, L., Le, L., Lanzirotti, A., Langenhorst, F., Krot, A.N., Keller, L.P., Kearsley, A.T., Joswiak, D., Jacob, D., Ishii, H., Harvey, R., Hagiya, K., Grossman, L., Grossman, J.N., Graham, G.A., Gounelle, M., Gillet, P., Genge, M.J., Flynn, G., Ferroir, T., Fallon, S., Ebel, D.S., Dai, Z.R., Cordier, P., Clark, B., Chi, M.F., Butterworth, A.L., Brownlee, D.E., Bridges, J.C., Brennan, S., Brearley, A., Bradley, J.P., Bleuet, P., Bland, P.A., Bastien, R., 2006. Report - mineralogy and petrology of comet 81P/Wild 2 nucleus samples. Science 314, 1735–1739. https://doi.org/10.1126/science.1135842.